Daytime Multilayered Cloud Detection Using Multispectral Imager Data

SHAIMA L. NASIRI

University of Wisconsin—Madison, Madison, Wisconsin

BRYAN A. BAUM

NASA Langley Research Center, Hampton, Virginia

(Manuscript received 1 December 2003, in final form 8 March 2004)

ABSTRACT

This study reports on recent progress toward the daytime detection of multilayered clouds in satellite multispectral data, specifically for the case of optically thin cirrus overlying lower-level water clouds. The technique is applied to 200 × 200 pixel arrays of data from the Moderate Resolution Imaging Spectroradiometer (MODIS) and is primarily based on the relationship between the near-infrared reflectance (at either 1.6 or 2.1 μm) and the 11-μm brightness temperature. Additional information used by the algorithm includes the operational MODIS cloud mask and cloud thermodynamic phase as inferred from the 8.5- and 11-μm brightness temperatures. The performance of the algorithm is evaluated for two MODIS case studies, and results are compared to coincident cloud physics lidar (CPL) data obtained from an aircraft platform. In both cases, the multilayered cloud detection algorithm results appear reasonable in comparison with the CPL data. The first case study, from 11 December 2002 during the *Terra–Aqua* Experiment (TX-2002), also examines the behavior of the algorithm when midlevel or mixed-phase cloud is present. The second case study, from 26 February 2003 during The Observing System Research and Predictability Experiment (THORPEX) campaign, sheds light on the sensitivity of the algorithm to optically thin cirrus. In this case, the algorithm does not detect cirrus with a visible (0.564 μm) optical thickness of less than 0.1 when it overlies a lower-level water cloud.

1. Introduction

Ground-based radar and lidar have demonstrated that multiple, overlapping cloud layers occur frequently (cf. Mace and Benson-Troth 2002; Uttal et al. 1995; Intrieri et al. 2002). Current operational satellite cloud retrieval efforts assume a priori that only single-layered clouds exist in a single field of view. This assumption is made necessary by the vast amounts of data collected by the satellite imagers, the available computing resources, the scientific objectives, and the need to process data quickly. With improved imager spatial and spectral resolution and increased computer resources, the consideration of multilayered clouds in satellite remote sensing becomes feasible. For example, González et al. (2002) use Along Track Scanning Radiometer (ATSR-2) data to study a case in which thin cirrus is known to overlay lower-level water cloud, and infer the cloud-top properties of both cloud layers.

When multiple cloud layers exist in a vertical column and a single-cloud-layer assumption is imposed on a retrieval of cloud pressure, the resulting cloud pressure tends to be in between the two cloud layers (e.g., Baum and Wielicki 1994). If the cloud pressure is incorrect, the retrieved cloud microphysical and optical properties may also be incorrect (e.g., Chung et al. 2000).

The purpose of this study is to present a straightforward method to discriminate satellite imager pixels in daytime data that potentially contain thin cirrus overlying a lower-level water cloud from those that contain single-layered clouds. The application of this method is based on radiances measured by the Moderate Resolution Imaging Spectroradiometer (MODIS) instrument, currently flown on the National Aeronautics and Space Administration (NASA) Earth Observing System *Terra* and *Aqua* platforms. The objective of this study is to reduce the number of erroneous retrievals by filtering out those pixels that may have more than one cloud layer. This method provides a way to ascertain the percentage of data in a given daytime scene that may contain cirrus over a lower-level water cloud.

The theoretical basis for the approach is described by Baum and Spinhirne (2000), who applied a cloud overlap discrimination method to a high-resolution (50 m) MODIS Airborne Simulator (MAS) scene with optically thin cirrus above a low-level water cloud. Their methodology was based on two generalizations regarding clouds. The first generalization is that ice crystals absorb

Corresponding author address: Shaima L. Nasiri, University of Wisconsin—Madison/CIMSS, 1225 W. Dayton St., Madison, WI 53706.
E-mail: shaima@ssec.wisc.edu

more radiation at a near-infrared wavelength, such as 1.6 μm, than do water droplets and therefore tend to be less reflective than water clouds at 1.6 μm. The second generalization is that ice clouds tend to reside higher in the atmosphere than water clouds; hence opaque ice clouds have lower 11-μm brightness temperatures. The specific assumptions invoked by Baum and Spinhirne (2000) were that

1) at most two distinct cloud layers were present in an array of data,
2) any pixels not uniquely associated with either of the two distinct cloud layers were classified as containing potential multilayered clouds,
3) the uppermost cloud layer was ice and the lower-level cloud layer was composed of liquid water, and
4) a separation distance of at least 2 km in height existed between the layers.

In our study, the approach of Baum and Spinhirne (2000) is modified for application to MODIS data (1-km spatial resolution) as follows. First, the operational MODIS cloud mask provides information regarding clear and cloudy pixels. Second, cloud thermodynamic phase is assessed using the 8.5- and 11-μm brightness temperatures (MODIS bands 29 and 31, respectively). Third, both the 1.6- and 2.1-μm reflectance bands (MODIS bands 6 and 7, respectively) are found to be useful in the multilayered cloud detection technique. The imaginary part of the index of refraction is higher for ice than for water in each of these bands. The 2.1-μm band is used for the *Aqua* data because a number of the 1.6-μm-band detectors on the *Aqua* MODIS instrument are inoperative (the band comprises 20 total detectors). Fourth, we propose a way to provide a confidence level to our assessment of whether a pixel contains more than one cloud layer. The confidence level is determined through a process of moving a pixel array, or tile, across the data granule, and testing each pixel (away from the granule borders) multiple times. In this fashion, a pixel may be flagged multiple times as containing multiple cloud layers. This tiling approach increases the likelihood that the algorithm will detect multilayered clouds.

An outline of the paper is as follows. The MODIS instrument, data products, and methodology are described in detail in section 2. Section 3 applies the methodology to two case studies and compares the results to coincident aircraft-based cloud lidar measurements. The results are summarized in section 4.

2. Data and algorithms

The multilayered cloud detection algorithm can be summarized as follows. A given block of 200 pixels by 200 pixels of MODIS data is separated into clear, cloudy, or uncertain pixels using the MODIS cloud mask (Ackerman et al. 1998). Subsequently, two groups of cloudy pixels are identified: pixels that are thought to belong uniquely to a single water cloud layer and those that belong to a single ice cloud layer. From the 2.1-μm reflectances (R[2.1]) and 11-μm brightness temperatures (BT[11]) of the single-layer ice and water cloud pixels, we infer a range of BT[11] and R[2.1] values within which multilayered, overlapping cloud pixels are expected to fall. This technique is applied sequentially to the entire MODIS image. We refine this technique by classifying each pixel multiple times using different sets of cloud statistics. Each step of the algorithm is explained in more detail below.

a. The MODIS instrument

MODIS is a 36-band whiskbroom-scanning radiometer (Barnes et al. 1998) located on two platforms: *Terra,* launched in 1999, and *Aqua,* launched in 2002. MODIS provides global coverage every 2 days from a polar-orbiting, sun-synchronous platform at an altitude of ~700 km. *Terra* is in a descending orbit with an equatorial crossing of 1030 UTC local solar time; *Aqua* is in an ascending orbit with a local solar time of 1330 UTC. In the MODIS nomenclature, the measured spectral regions are referred to as ''bands,'' and within each band there are detector arrays that are referred to as ''channels.'' The bands are distributed between 0.415 and 14.235 μm in four focal plane assemblies, with nadir spatial resolutions of 250 (2 bands), 500 (5 bands), and 1000 m (29 bands). The 250-m bands are at wavelengths of 0.65 and 0.86 μm, while the 500-m bands are provided at wavelengths of 0.47, 0.56, 1.2, 1.6, and 2.1 μm. The cloud overlap detection uses 1-km-resolution MODIS data, which implies that bands with subkilometer resolution, that is, 0.415–2.15 μm, have been aggregated into 1-km-equivalent pixels. These aggregated bands have been collocated with the other twenty-nine 1-km bands and archived in a common file in which all bands have a 1-km-equivalent spatial resolution.

b. Cloud clearing

The MODIS cloud mask is produced globally over all surfaces and illumination conditions at a 1-km and 250-m pixel resolution. The various tests employ as many as 14 of the 36 MODIS spectral bands to maximize reliable cloud detection (Ackerman et al. 1998; Platnick et al. 2003). The purpose of the cloud mask is to assess the likelihood of a pixel being obstructed by clouds or thick aerosols. The product provides information on individual cloud test results, the processing path, and ancillary information. The mask is designed to allow for varying degrees of clear-sky confidence by combining the results from the various spectral and spatial tests into the following four categories: *confident clear, probably clear, uncertain*/*probably not clear,* and *not clear.* In most cases, *not clear* will mean that the field of view is cloud covered, although in some cases

the obstruction could be due to optically thick aerosols. This confidence assessment is provided in the first two bits of the mask product. Further details may be found in the above references. Pixels characterized by the cloud mask product as *not clear* are considered cloudy for the purpose of the overlapping cloud detection. Only these cloudy pixels have the potential to be classified as overlapped by the algorithm. Those pixels characterized as *confident clear* by the cloud mask are considered to be clear by the multilayered cloud detection algorithm and are used to generate the clear-sky statistics described in section 2d. Our algorithm considers pixels characterized as *probably clear* or *uncertain*/*probably not clear* by the cloud mask to be uncertain. Our algorithm neither uses nor attempts to classify these uncertain pixels.

c. Single-layer cloud identification

The determination of pixels containing distinct ice or water clouds is based on the BT[11] and the brightness temperature difference between 8.5 and 11 μm (BTD[8.5–11]). The physical basis for the inference of cloud phase from these bands is the difference of microphysical and optical properties between water droplets and ice crystals (Strabala et al. 1994). Radiative transfer simulations (Baum et al. 2000) indicate that the BTD[8.5–11] values tend to be positive for ice clouds that have a visible optical thickness greater than approximately 0.5, but this depends on the surface emissivity at these IR wavelengths. Water clouds of relatively high optical thickness tend to exhibit negative BTD[8.5–11] values, typically less than -2 K. Radiative transfer calculations indicate that the BTD[8.5–11] is quite sensitive to atmospheric absorption, especially by water vapor. The BTD[8.5–11] value for lower-level clouds tends to become more negative as the water vapor loading increases in the column and as the surface emittance at 8.5 μm decreases.

For the purpose of detecting multilayered clouds, the BTD[8.5–11] test is employed to identify pixels that most likely contain single-layer ice clouds and single-layer water clouds. Because the single-layer cloud pixels serve as a seed for subsequent processing, the BTD[8.5–11] test is applied more rigorously than in the bispectral infrared MODIS cloud phase algorithm described by Platnick et al. (2003). Pixels with a strongly positive BTD[8.5–11] are classified as single-layer ice cloud and those with a strongly negative BTD[8.5–11] as single-layer water cloud. With our application of the BTD[8.5–11] tests, optically thin cirrus do not tend to be identified as single-layer ice cloud.

d. Multilayered cloud detection in a data array

The discrimination of pixels containing single-layered clouds from those containing multilayered clouds is performed on an array, or tile, of data. Each pixel within the tile contains the measured radiometric information as well as the results from the cloud mask and BTD[8.5–11]. Each tile of data consists of $N \times N$ pixels. For this study, we use data tiles of 200 $\times$ 200 pixels (approximately 40 000 km^2).

As in Baum and Spinhirne (2000), cloud layer discrimination is based on an analysis of the scatter diagram of data from a near-infrared (NIR; R[2.1]) and an IR (BT[11]) band. The current method differs from theirs in how cloud clearing and cloud thermodynamic phase is determined. While Baum and Spinhirne (2000) considered the coldest (lowest BT[11]) pixels to be single-layer ice cloud and the brightest pixels (highest R[1.6]) to be single-layer water cloud, we bring in a separate piece of information in the form of the BTD[8.5–11]. While the examples presented use the R[2.1] as the near-infrared reflectance band, no algorithm changes are necessary if the R[1.6] data are used instead.

Figure 1a shows a false-color phase image of a 200 $\times$ 200 pixel tile from *Aqua* MODIS on 11 December 2002 at 1915 UTC. In this false-color map, the 0.65-μm reflectance (R[0.65]) is mapped to red, the R[2.1] is mapped to green, and the BT[11] is mapped to blue, although with this IR band the values are inverted so that cold objects are bright. In the image, ice clouds appear as pink to purple, water clouds appear yellow to white, and land surfaces appear green. Figure 1b shows which pixels are classified by the cloud mask as clear (magenta), likely single-layer ice cloud by BTD[8.5–11] (green), and single-layer water cloud (cyan).

Figure 1c shows the scatter diagram of the 200 $\times$ 200 pixel tile in Fig. 1b with the individual pixels color-coded to provide the results from the cloud mask and single-layer cloud phase identification. For clarity, every third pixel is shown in the scatter diagram. Clear-sky pixels are magenta circles (corresponding to the magenta pixels in Fig. 1b), ice cloud pixels are green squares, and water cloud pixels are cyan circles. All other cloudy pixels from Fig. 1b are shown in gray.

The means and standard deviations of the BT[11] and R[2.1] are then calculated for the clear, single-layer ice cloud, and single-layer water cloud pixels. Figure 1c shows the locations of six points within the plane defined by the BT[11] and R[2.1] where the BT[11] is the abscissa and the R[2.1] the ordinate. Point C has the coordinates ($\overline{Clear_{11}}$, $\overline{Clear_{2.1}}$). In this notation, $\overline{Clear_{11}}$ refers to the mean BT[11] of the clear pixels. Similarly, point I is based on the single-layer ice cloud pixels and point W on the water cloud pixels. Because ice clouds are assumed to vary more as a function of the optical thickness in the BT[11], point I′ is defined as [$\overline{Ice_{11}}$, $\overline{Ice_{2.1}} + \sigma(Ice_{2.1})$]. Here $\sigma(Ice_{2.1})$ refers to the standard deviation of the R[2.1] of the single-layer ice pixels. Point W′ is defined as [$\overline{Water_{11}} - \sigma(Water_{11})$, $\overline{Water_{2.1}}$]. Point C′ is defined as the intersection of a line through I′ with the same slope as line IC and a line

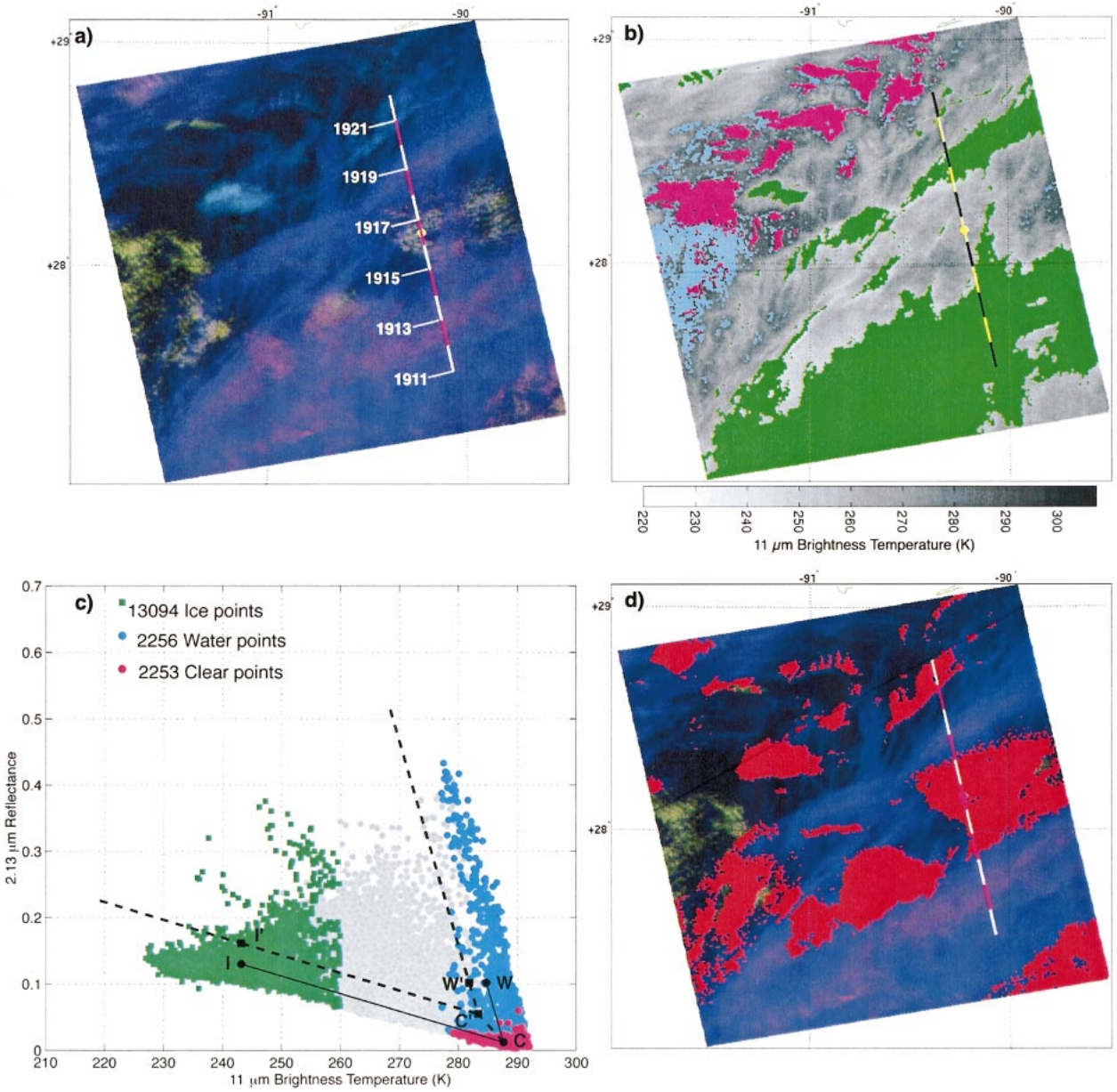

FIG. 1. A 200 × 200 pixel block of MODIS data from *Aqua* at 1915 UTC 11 Dec 2002. (a) A false-color phase image where the R[0.65] is mapped to red, R[2.1] is mapped to green, and BT[11] is mapped to blue. The dashed line running from south to north shows 11 min from the ER-2 flight track from 1911 to 1922 UTC. (b) The seed pixels from the cloud mask and the BTD[8.5–11] overlaid on the BT[11] image. Single-layer ice pixels are shown in green, single-layer water cloud pixels in cyan, and clear pixels in magenta. (c) These pixels shown as an R[2.1] vs BT[11] scatter diagram. (d) The pixels falling between the dashed lines in (c) are classified as multilayered and are shown in red.

through W′ with the same slope as line WC. These points allow the construction of lines I′C′ and W′C′. If the angle between the lines is large enough, the assumption of two cloud layers is made. In this case, all points that fall between the dashed lines are classified as potentially containing multilayered clouds. This includes those pixels within the dashed lines that may have originally been classified as single-layer water or ice clouds. The pixels classified as potentially multilayered in Fig. 1c are overlaid in red on the false-color phase image in Fig. 1d.

The following criteria must be met by the 200 × 200 tile before any pixels within the tile are processed to determine if multilayered clouds may be present:

1) pixels are present that are classified as *not clear* by the cloud mask,
2) at least 10 pixels are classified as *confident clear* by the cloud mask,

3) at least 10 cloud pixels are determined to be ice phase,
4) at least 10 pixels are determined to be liquid water phase, and
5) the angle between lines IC and WC in the scatter diagram (Fig. 1c) is greater than 20° (calculated with R[2.1] as percent reflectance).

If these five criteria are not met, then no effort is made to determine if multilayered clouds might be present within the tile. The minimum-angle rule helps to ensure that only tiles with two distinct cloud layers are considered. An array with two well-separated water cloud layers, for example, will undergo no further processing.

The entire 1915 UTC 11 December 2002 *Aqua* MODIS granule is shown in false color in Fig. 2a with the same false-color mapping as in Fig. 1a. The 200 × 200 pixel tile of Fig. 1a is highlighted in yellow in Fig. 2a. The multilayered clouds for this scene are shown in Fig. 2b. One problem to note is the tendency for blockiness in the results shown in Fig. 2b, which occurs because statistics are generated for fairly large tiles. For a single iteration through a granule of MODIS data, each pixel will be analyzed only once, and only when the above conditions are met. One potential solution is to employ a staggered tiling approach that analyzes each pixel more than once.

e. The tiling approach

To gain understanding regarding the reliability of the technique and to increase the likelihood that algorithm constraints will be met, we introduce a modification as follows. Instead of applying the technique to individual, nonoverlapping tiles ($N \times N$ pixels) over an image, the tiles are staggered over the image. To analyze each pixel up to 4 times, away from the granule boundaries, the tile is moved $N/2$ pixels both along track and cross track over the granule. Similarly, each pixel can be analyzed up to 16 times by moving each tile $N/4$ pixels successively over the granule. The issue at this point is one of keeping track of the number of times each pixel in the granule is identified as having multiple cloud layers.

Results are presented in Figs. 2c and 2d for the cases in which each pixel is analyzed up to 16 and 100 times, respectively. These results are generated for $N = 200$. From comparison of Figs. 2c and 2d with the results of a single pass through the data in Fig. 2b, one gains a sense of the robustness of the approach. The amount of multilayered cloud found increases noticeably between the single-pass results in Fig. 2b and the 16-pass results in Fig. 2c. The increase in the multilayered cloud detection from 16 to 100 passes (in Fig. 2d) is less notable, but the blockiness is decreased.

The tiling approach has two benefits in terms of product quality. The first benefit is a reduction in the blockiness of the results. The second benefit is that one may attach a higher level of confidence to those pixels identified as containing multilayered clouds. For example, a higher confidence level may be given to those pixels for which multilayered clouds are detected in more than 20 out of 100 passes.

3. Case studies

This section describes two case studies demonstrating the performance of the multilayered cloud detection algorithm. The first case is of an *Aqua* MODIS granule over the Gulf of Mexico on 11 December during the 2002 *Terra–Aqua* Experiment (TX-2002). Also an *Aqua* scene, the second case is from 26 February 2003 during The Observing System Research and Predictability Experiment (THORPEX) observing system test. These particular scenes have been chosen because of the availability of MODIS *Terra* or *Aqua* scenes coincident with cloud physics lidar (CPL) (McGill et al. 2002) data aboard the NASA ER-2. For each case, the performance of the multilayered cloud detection algorithm is demonstrated.

a. TX-2002: 11 December 2002

An *Aqua* cloud product validation mission was conducted on 11 December 2002 during TX-2002. The NASA ER-2 launched from San Antonio, Texas, at 1700 UTC and landed at 2130 UTC. The ER-2 underflew the *Aqua* satellite over the Gulf of Mexico at 1916 UTC. The MAS, described by King et al. (1996), and the CPL were among the aircraft instruments that collected data during this flight. For this case study, ER-2 data use is limited to the 5 min prior to and following the 1916 UTC underflight of *Aqua* in order to minimize scene differences due to cloud motion and/or cloud life cycle. The CPL cloud heights and winds from the 0000 UTC 12 December 2002 sounding from Lake Charles, Louisiana, are used to estimate potential spatial errors between clouds observed by the ER-2 along the flight line and those observed by MODIS. We estimate the maximum horizontal spatial error (at 1911 and 1921 UTC) between ER-2-observed cloud and MODIS clouds to be approximately 11.5 km for high clouds and 2.3 km for low clouds; these errors are based on the time differences and wind speeds at the two cloud heights. This error should be minimal at the 1916 UTC underflight of MODIS.

Figure 1a shows a 200 km × 200 km false-color phase image with the ER-2 flight track superimposed. The 1916 UTC underflight point with *Aqua* is marked in yellow. Alternating magenta and white lines show each minute of the ER-2 flight track starting in the south at 1911 UTC and ending in the north at 1922 UTC. From the false-color phase image, one may infer that from 1911 to 1915 UTC, the ER-2 flight track is over cirrus of varying optical thickness or temperature. From 1915 to about 1918 UTC, the flight track is over thin cirrus overlying lower-level water cloud. From about 1918:00

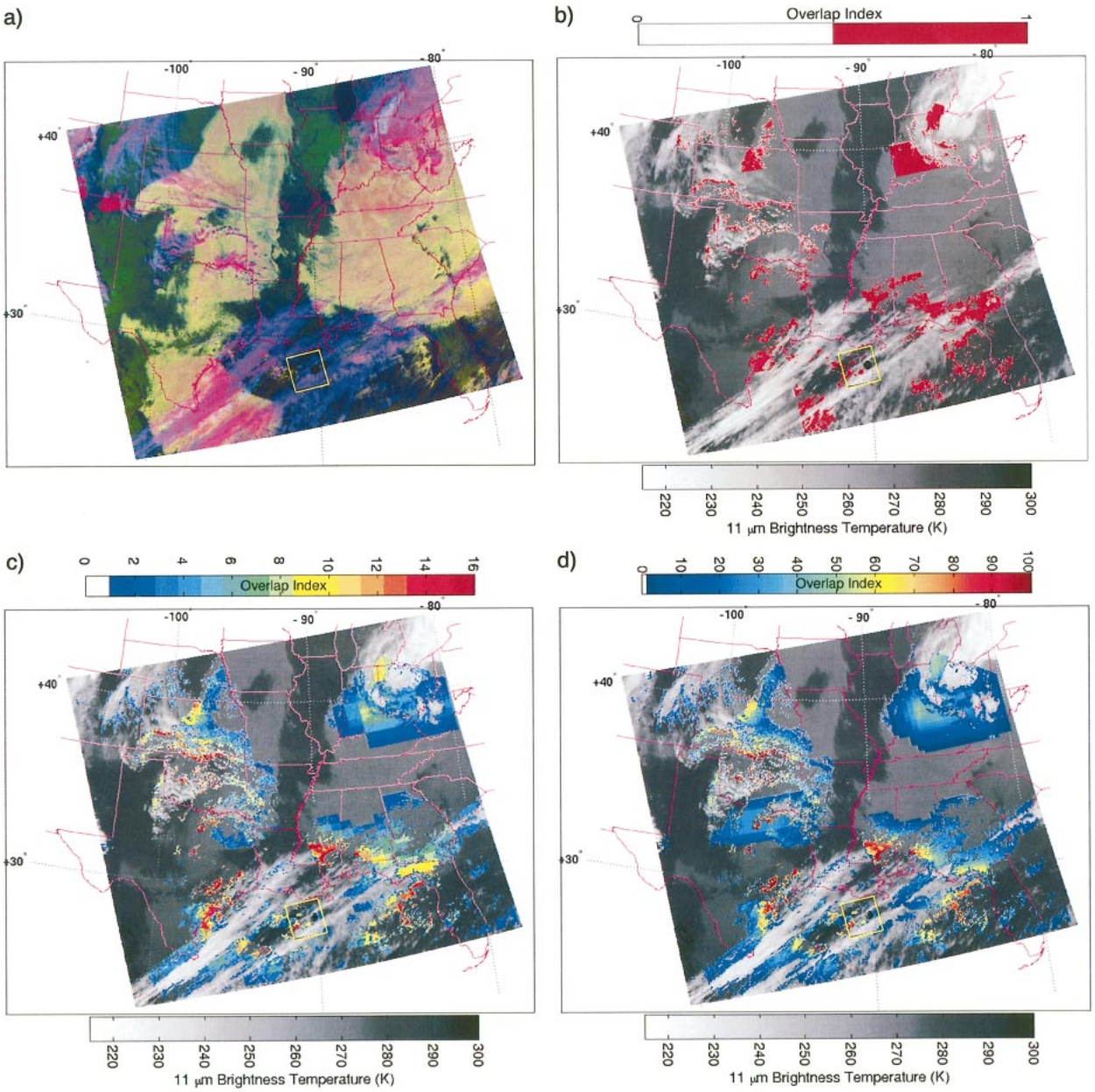

FIG. 2. The full MODIS data from *Aqua* at 1915 UTC 11 Dec 2002. The region in the Gulf of Mexico outlined in yellow is the 200 × 200 pixel subset shown in Fig. 1. (a) The false-color phase colormap. (b), (c), (d) The multilayered clouds superimposed upon the grayscale BT[11] image with 1, 16, and 100 overpasses, respectively.

to 1919:30 UTC, the ER-2 is again over cirrus, with no visual evidence of a lower-level water cloud. The cloud from about 1920:30 to 1922:00 UTC is more difficult to classify; additional information is necessary in this case.

Cloud boundaries from the CPL are shown in Fig. 3a. According to the lidar, a cirrus layer with a cloud-top height between 11 and 12 km and cloud base between 8 and 10 km (not considering layer separations $\leq$0.5 km) is present from 1911 to 1922 UTC. A cloud at about 1 km is also present from 1914:00 to 1917:40 UTC, with a few breaks between 1914:30 and 1915:20 UTC. Also, two cloud layers separated by about 1 km are present from 1920:20 to 1922:00 UTC with cloud tops near 9 and 11 km. Figure 3b shows the CPL-retrieved optical thickness at 532 and 1064 nm (τ_{532} and τ_{1064}, respectively) within the layer specified by Fig. 3c for the same time period. The CPL optical thickness retrievals are considered to be reliable only up to an optical thickness of about 2.5. From 1920:15 to 1922:00 UTC, there are periods when the optical thickness is too great and is therefore not retrieved.

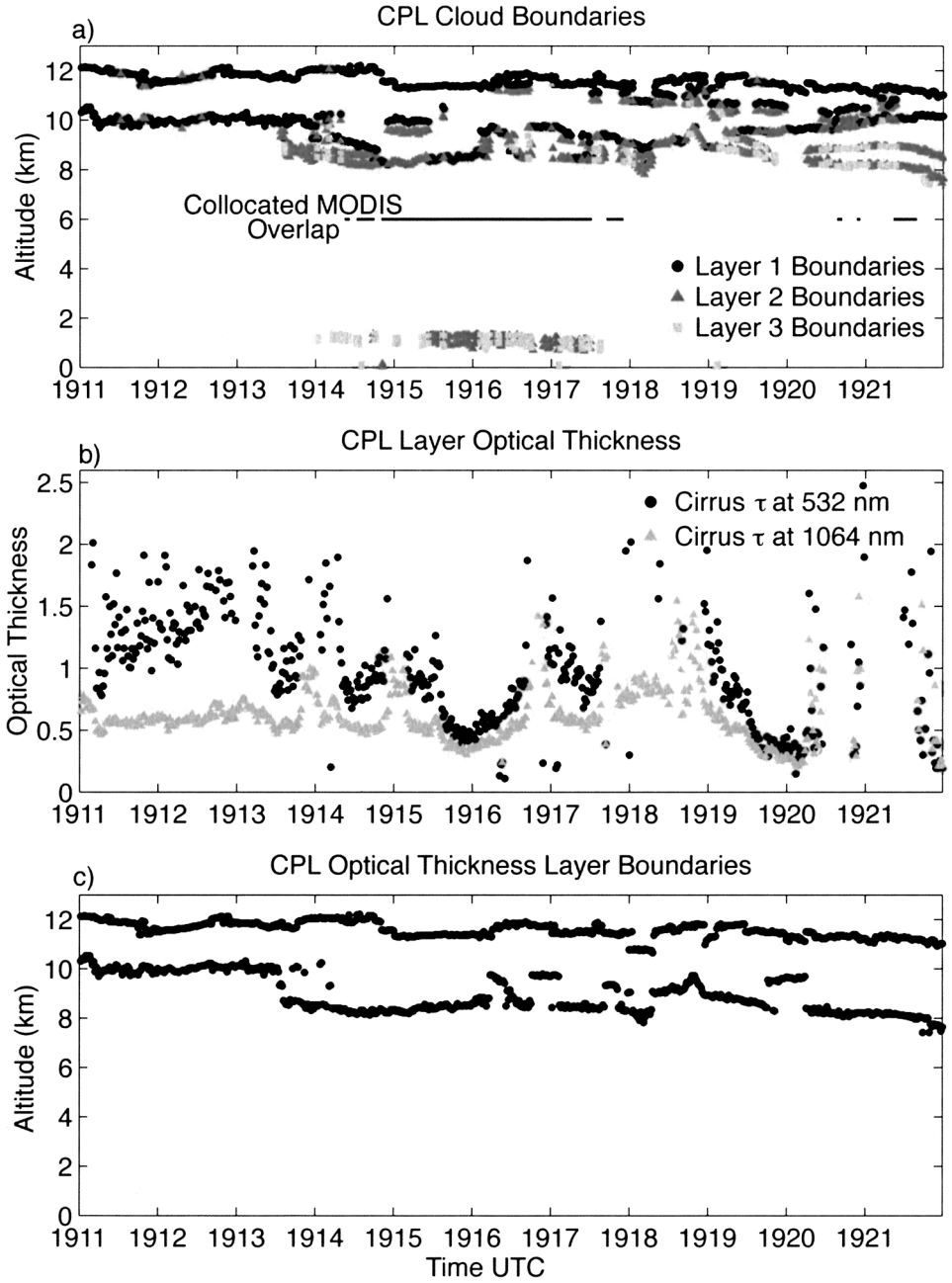

FIG. 3. (a) CPL cloud boundaries from 1911 to 1922 UTC show consistent high cloud cover throughout the time period, as well as scattered low cloud between 1914 and approximately 1918 UTC. Collocated MODIS pixels with high confidence of the presence of multilayered clouds are shown at 6 km. (b) Retrieved CPL cirrus optical thickness for the cloud layer shown in (c).

The CPL cloud-layer information can be compared to the MODIS multilayered cloud detection results shown in Fig. 1d. MODIS pixels with a high confidence of cloud overlap and collocated with the CPL are shown at 6 km in Fig. 3a. The analysis shows that areas likely containing thin cirrus overlaying lower-level water cloud occur along the flight line from about 1914 to 1918 UTC and from about 1920:50 to 1922:00 UTC. The multilayered clouds found between 1914 and 1918 UTC compare well with visual inspection of the false-color phase image (Fig. 1a) and the lidar cloud boundary information (Fig. 3a). While it is tempting to relate the multilayered cloud results from 1921 to 1922 UTC to the presence of two cloud layers shown in the lidar imagery, it should be noted that the upper-level cirrus cloud optical thickness from the lidar is less than 0.1.

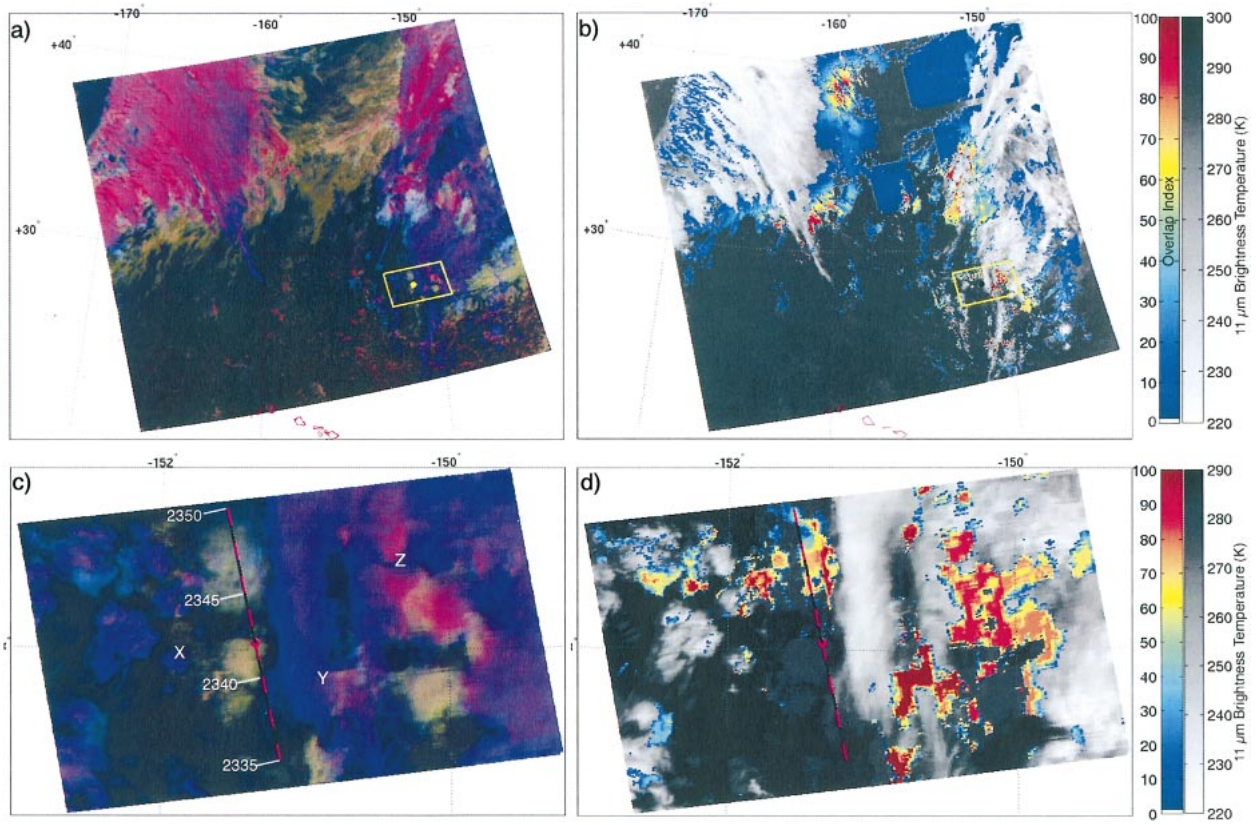

FIG. 4. *Aqua* MODIS 2340 UTC 26 Feb 2003 data. The full granule false-color image (same colormap as in Fig. 1a) is shown in (a). The yellow outline on the right-hand side marks the boundaries of the 200 × 200 pixel blocks shown in (c) and (d). (b) The 100-pass multilayered cloud product is superimposed on the BT[11] image. Multilayer cloud indices greater than about 20 indicate a high likelihood of overlapping clouds. (c) A 200 × 200 pixel false-color image centered on the ER-2 underflight point (magenta circle). The magenta and black dashed line running from south to north shows 15 min from the ER-2 flight track from 2335 to 2350 UTC. (d) The 200 × 200 pixel subset of (b).

While optical thickness sensitivity modeling should be performed to determine the sensitivities of the overlap detection to optical thickness and temperature separation, 0.1 will almost certainly fall outside of the detection range. A much more likely possibility, based on the lidar depolarization ratio (not shown), is that the cloud at 9 km contains some amount of liquid water as well as some ice particles. Single-layered but mixed-phase clouds are sometimes classified as multilayered clouds by the algorithm when there are other distinct ice and water cloud layers present elsewhere within the $N \times N$ pixel block; that is, the assumption for a pixel array is that there are at most two distinct cloud layers, not three. Further work is being performed to minimize this classification error.

b. THORPEX: 26 February 2003

On 26 February 2003, an *Aqua* cloud product validation mission was conducted out of Hickam Air Force Base in Honolulu, Hawaii. The ER-2 launched at 2200 UTC and landed at 0320 UTC (27 February 2003). At 2342 UTC the ER-2 obtained coincident measurements with the *Aqua* satellite along a flight track parallel to the satellite suborbital track, but offset by about 500 km, corresponding to a 40° satellite view angle. The CPL and the MAS were among the ER-2 platform instruments that collected data. The ER-2 data are limited to the 7 min prior to and 8 min following the 2342 UTC underflight to minimize scene differences between the aircraft instruments and MODIS. With the use of CPL cloud heights and the Lihue, Hawaii, sounding from 0000 UTC 27 February 2003, the potential horizontal spatial offsets between the location of clouds observed by the ER-2 and the MODIS can be estimated. This offset could be as large as 19 km for high clouds and 2 km for low clouds at the beginning (2335 UTC) and end (2350 UTC) of the ER-2 flight track.

The entire MODIS granule from 2340 UTC is shown in Fig. 4a; the color map is the same as in Fig. 1a. Optically thick ice clouds are present in the northwest quadrant of the image and along the eastern edge of the granule. Lower-level water cloud covers much of the northern half of the image. The Hawaiian Islands can be seen to the south. The 100-pass multilayered cloud detection product is overlaid upon the BT[11] in Fig. 4b. Regions with a high confidence of multilayered

clouds (having indices greater than 20) are found along the edges of the cirrus deck.

A 200 × 200 pixel block centered around the 2342 UTC ER-2 underflight point is outlined in yellow in Fig. 4a and shown in more detail in Fig. 4c. The ER-2 flight line is also shown in Fig. 4c starting in the south at 2335 UTC and ending in the north at 2350 UTC. The false-color image provides information about cloud phase and multilayered clouds. Along the flight track, a high-level cloud is visible from 2336 to 2340 UTC and a lower-level cloud is visible from 2340 to 2342 UTC. Two cloud layers are present from 2344 to 2349 UTC. On the right-hand side of the image, high satellite viewing angle effects are visible. Other regions of multilayered clouds are present in Fig. 4c at the locations marked X, Y, and Z. This visual inspection of the false-color phase product compares well with much of the multilayered cloud product image in Fig. 4d. The multilayered cloud detection along the flight track between 2345 and 2350 UTC also compares reasonably well with the MAS imagery (not shown).

Cloud boundaries from the CPL are shown in Fig. 5a. Collocated MODIS pixels with a high confidence of multilayered clouds are shown at 5 km. The CPL data indicate that a cirrus layer with a top between 10 and 11 km and base between 8 and 9 km (not considering layer separations $\leq$0.5 km) is present from 2335 to 2343 UTC. A low-level cloud at 1 km seems to be present from 2340 to 2349 UTC, with a few breaks around 2340, 2343, and 2344 UTC. Because no low cloud is apparent in either the MODIS or the MAS visible imagery and the CPL retrieved cloud base is at the surface, the CPL result at 1 km between 2335 and 2338 UTC is likely indicative of an aerosol layer rather than a low cloud. A physically thin cloud layer is also present at about 7 km from 2343 to 2350 UTC. Figure 5b shows the CPL-retrieved τ_{532} and τ_{1064} within the layer specified by Fig. 5c for the same time period. The CPL optical thickness retrievals are considered to be reliable only up to an optical thickness of about 2.5. After 2344 UTC, there are periods when optical thickness is not retrieved by the CPL due to detector saturation within the cloud at 7 km.

One question to ask is why no multilayered clouds are found in the MODIS data between 2340 and 2342 UTC, as the ER-2 pilot described the scene at the underflight point (2342 UTC) as one of thin wispy cirrus over lower-level cloud. The CPL-retrieved optical thickness may provide some insight to this question. Between 2340 and 2342 UTC the lidar τ_{532} and τ_{1064} ranges between just above 0 and 0.2. This is similar to the retrieved lidar optical thickness between 2335 and 2336 UTC, a time period that the MODIS cloud mask characterizes as *confident clear*. The cirrus optical thickness seems to be below the sensitivity of our technique to work with reliably.

4. Summary and conclusions

This study describes a method to detect thin cirrus overlaying lower-level water clouds in daytime multispectral MODIS imager data. As first described by Baum and Spinhirne (2000), the technique exploits two generalizations about clouds: 1) at near-infrared wavelengths (e.g., 2.1 μm) ice particles tend to absorb more radiation than water droplets, and 2) as ice clouds generally reside higher in the atmosphere than water clouds, they tend to have lower brightness temperatures in the infrared window (i.e., 11 μm) than water clouds. Together with these generalizations, the identification of clear pixels and single-layer ice and water cloud pixels makes it possible to discriminate single-layered from multilayered cloud pixels.

This study expands upon the work of Baum and Spinhirne (2000) and demonstrates a multilayered cloud detection algorithm for the MODIS instrument. Four primary modifications are proposed to the aforementioned technique. First, we work with $N \times N$ (usually 200 × 200) tiles of MODIS data. Second, cloud clearing is performed using the operational MODIS cloud mask. Third, cloud thermodynamic phase determination and identification of single-layer cloud pixels is based upon analysis of the infrared window data in the 8.5- and 11-μm bands. Finally, each pixel is evaluated multiple times for the presence of multilayered clouds by staggering the data tile over the image.

Two case studies are presented and the results are compared to coincident aircraft-based cloud lidar data. In both cases, the multilayered cloud detection algorithm results are reasonable in comparison with the CPL data. The first case study, from 11 December 2002 during the TX-2002 experiment, also shows the behavior of the algorithm when midlevel or mixed-phase cloud is present. In this case, midlevel cloud is classified as most likely multilayered by the algorithm, perhaps incorrectly. The second case study, from 26 February 2003 during the THORPEX campaign, sheds light on the sensitivity of the algorithm to optically thin cirrus. In this case, the algorithm does not detect cirrus with an optical thickness at 0.564 μm of approximately 0.1 when it overlies a lower-level water cloud.

In future work, the ability to identify scenes with thin cirrus overlaying a lower-level water cloud in a global satellite dataset will enable estimations of the spatial extent of multilayered clouds and biases in remotely sensed cloud properties due to their occurrence. To further this goal, we are further refining the method to better identify which of the pixels classified as multilayered are actually single-layered, possibly mixed-phase clouds.

Acknowledgments. The authors gratefully acknowledge the support of the CPL and MODIS Science Teams. The first author's graduate study was supported by a

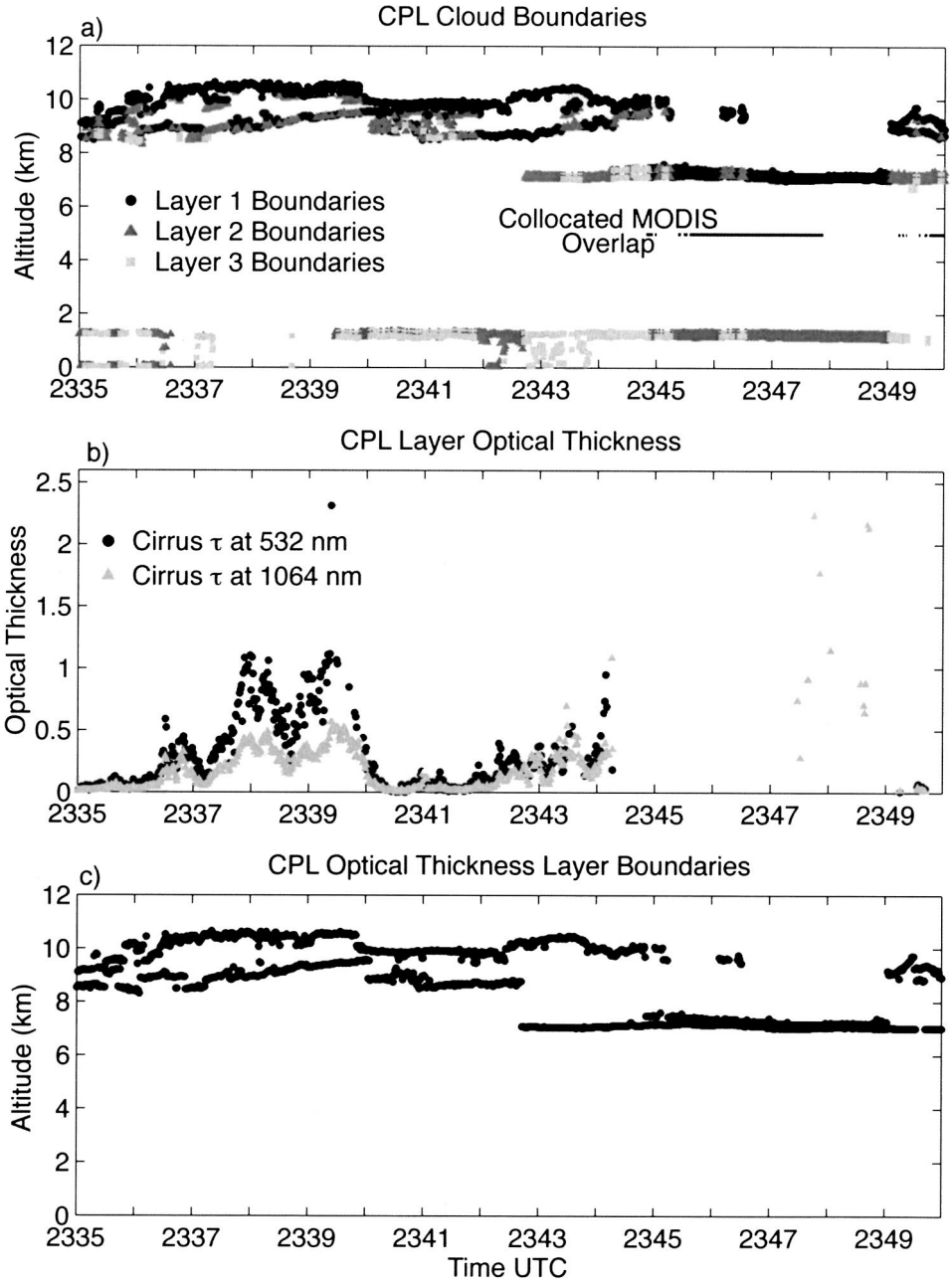

FIG. 5. (a) CPL cloud boundaries from 2335 to 2350 UTC show consistent high cloud cover throughout the time period, as well as low cloud throughout much of the flight. Collocated MODIS pixels with high confidence of multilayered clouds are shown at 5 km. (b) Retrieved CPL cirrus optical thickness at 532 and 1064 nm for the cloud layer shown in (c).

NASA GSFC Earth Sciences Directorate Suomi–Simpson Fellowship. The authors also acknowledge the support of the CERES Science Team and the Biological and Environmental Research Program (BER) in the U.S. Department of Energy (Interagency Agreement DE-AI02-00ER62901) during the early development of this work.

REFERENCES

Ackerman, S. A., K. I. Strabala, W. P. Menzel, R. A. Frey, C. C. Moeller, and L. E. Gumley, 1998: Discriminating clear sky from clouds with MODIS. *J. Geophys. Res.*, **103,** 32 141–32 157.

Barnes, W. L., T. S. Pagano, and V. V. Salomonson, 1998: Prelaunch characteristics of the moderate resolution imaging spectroradiometer (MODIS) on EOS-AMI. *IEEE Trans. Geosci. Remote Sens.*, **36,** 1088–1100.

Baum, B. A., and B. A. Wielicki, 1994: Cirrus cloud retrieval using infrared sounding data: Multilevel cloud errors. *J. Appl. Meteor.,* **33,** 107–117.

——, and J. D. Spinhirne, 2000: Remote sensing of cloud properties using MODIS Airborne Simulator imagery during SUCCESS. III. Cloud overlap. *J. Geophys. Res.,* **105,** 11 793–11 804.

——, P. F. Soulen, K. I. Strabala, M. D. King, S. A. Ackerman, and W. P. Menzel, 2000: Remote sensing of cloud properties using MODIS Airborne Simulator imagery during SUCCESS. 2. Cloud thermodynamic phase. *J. Geophys. Res.,* **105,** 11 781–11 792.

Chung, S., S. Ackerman, and P. F. van Delst, 2000: Model calculations and interferometer measurements of ice-cloud characteristics. *J. Appl. Meteor.,* **39,** 634–644.

González, A., P. Wendling, B. Mayer, J.-F. Gayet, and T. Rother, 2002: Remote sensing of cirrus cloud properties in the presence of lower clouds: An ATSR-2 case study during the interhemispheric differences in cirrus properties from anthropogenic emissions experiment. *J. Geophys. Res.,* **107,** 4693, doi: 10.1029/2002JD002535.

Intrieri, J. M., M. D. Shupe, T. Uttal, and B. J. McCarty, 2002: An annual cycle of arctic cloud characteristics observed by radar and lidar at SHEBA. *J. Geophys. Res.,* **107,** 8030, doi:10.1029/2000JC000423.

King, M. D., and Coauthors, 1996: Airborne scanning spectrometer for remote sensing of cloud, aerosol, water vapor, and surface properties. *J. Atmos. Oceanic Technol.,* **13,** 777–794.

Mace, G. G., and S. Benson-Troth, 2002: Cloud-layer overlap characteristics derived from long-term cloud radar data. *J. Climate,* **15,** 2505–2515.

McGill, M., D. Hlavka, W. Hart, V. S. Scott, J. Spinhirne, and B. Schmid, 2002: Cloud physics lidar: Instrument description and initial measurement results. *Appl. Opt.,* **41,** 3725–3734.

Platnick, S., M. D. King, S. A. Ackerman, W. P. Menzel, B. A. Baum, J. C. Riédi, and R. A. Frey, 2003: The MODIS cloud products: Algorithms and examples from Terra. *IEEE Trans. Geosci. Remote Sens.,* **41,** 459–473.

Strabala, K. I., S. A. Ackerman, and W. P. Menzel, 1994: Cloud properties inferred from 8–12-μm data. *J. Appl. Meteor.,* **33,** 212–229.

Uttal, T., E. E. Clothiaux, T. P. Ackerman, J. Intrieri, and W. L. Eberhard, 1995: Cloud boundary statistics during FIRE-II. *J. Atmos. Sci.,* **52,** 4276–4284.